Patch2Self denoising of Diffusion MRI with Self-Supervision and Matrix Sketching

Shreyas Fadnavis[*,a], Agniva Chowdhury[b], Joshua Batson[c], Petros Drineas[d], Eleftherios Garyfallidis[a]

[a]*Intelligent Systems Engineering, Indiana University Bloomington, USA*
[b]*Department of Statistics, Purdue University, USA*
[c]*Chan Zuckerberg Biohub*
[d]*Department of Computer Science, Purdue University, USA*

Abstract

Diffusion-weighted magnetic resonance imaging (DWI) is the only noninvasive method for quantifying microstructure and reconstructing white-matter pathways in the living human brain. Fluctuations from multiple sources create significant additive noise in DWI data which must be suppressed before subsequent microstructure analysis. We introduce a self-supervised learning method for denoising DWI data, Patch2Self (P2S), which uses the entire volume to learn a full-rank locally linear denoiser for that volume. By taking advantage of the oversampled q-space of DWI data, P2S can separate structure from noise without requiring an explicit model for either. The setup of P2S however can be resource intensive, both in terms of running time and memory usage, as it uses all voxels (n) from all-but-one held-in volumes ($d-1$) to learn a linear mapping $\Phi : \mathbb{R}^{n\times(d-1)} \mapsto \mathbb{R}^n$ for denoising the held-out volume. We exploit the redundancy imposed by P2S to alleviate its performance issues and inspect regions that influence the noise disproportionately. Specifically we introduce P2S-sketch, which makes a two-fold contribution: *(1)* P2S-sketch uses matrix sketching to perform self-supervised denoising. By solving a sub-problem on a smaller sub-space, so called, *coreset*, we show how P2S can yield a significant speedup in training time while using less memory. *(2)* We show how the so-called statistical leverage scores can be used to *interpret* the denoising of dMRI data, a process that was traditionally treated as a black-box. Our experiments conducted on simulated and real data clearly demonstrate that P2S via matrix sketching (P2S-sketch) does not lead to any loss in denoising quality, while yielding significant speedup and improved memory usage by training on a smaller fraction of the data. With thorough comparisons on real and simulated data, we show that Patch2Self outperforms the current state-of-the-art methods for DWI denoising both in terms of visual conspicuity and downstream modeling tasks. We demonstrate the effectiveness of our approach via multiple quantitative metrics such as fiber bundle coherence, R^2 via cross-validation on model fitting, mean absolute error of DTI residuals across a cohort of sixty subjects.

Key words: Diffusion MRI, denoising, self-supervised learning, Randomized Numerical Linear Algebra, Matrix Sketching

1. Introduction

Diffusion MRI (dMRI) is a 4D acquisition method that generates a series of 3D volumes each corresponding to different gradient directions [6, 44]. Each 3D volume provides unique information about the underlying diffusion processes in the brain. This information is used to probe the tissue microstructure in the living brain by modeling the signal per voxel using a variety of biophysical models [64, 65]. This derived information can however be corrupted due to low signal-to-noise ratio (SNR). Multiple sources of noise are apparent in dMRI that reduce SNR. Furthermore, with new acquisition schemes, high-field MR gradients [80, 61] and multi-dimensional diffusion encoding strategies [71, 41] the effect of noise sources is exaggerated and affects image conspicuity.

In the past, denoising dMRI has been tackled using a variety of methods belonging to different classes based on the signal assumptions imposed. The first class of denoising methods used for DWI data were extensions of techniques developed for 2D images, such as non-local means (NL-means) [17] and its variants [16, 12]), total variation norm minimization [46], cosine transform filtering [57], empirical Bayes [3] and correlation based joint filtering [79]. Some other methods take more direct advantage of the fact that DWI measurements have a special 4D structure, representing many acquisitions of the same 3D volume at different b-values and in different gradient directions. Assuming that small spatial structures are more-or-less consistent across these measurements, these methods project to a local low-rank approximation of the data [66, 58]. The top performing methods are overcomplete Local-PCA (LPCA) [58] and its Marchenko-Pastur extension [81]. The current state-of-the-art unsupervised method for denoising DWI is the Marchenko-Pastur PCA, which handles the choice of rank in a principled way by thresholding based on the eigenspectrum of the expected noise covariance matrix. Note that Marchenko-Pastur PCA, like the classical total variation norm and NL-means methods, requires a noise model (via the Marchencko-Pastur distribution) to do the denoising, either as an explicit standard deviation and covariance as in LPCA, or implicitly in the choice of a noise correction method [47, 76].

Self-supervised learning, as a sub-domain of unsupervised

[*]Corresponding author

learning algorithms, has been rapidly gaining traction over the past years. Novel strategies of self-supervision are being developed and employed for different problems such as multimodal learning [86, 62], self-labeling [56, 48], learning semantic context [19] and contrastive predictive coding [4]. Denoising strategies based on self-supervision have revolutionized image denoising performance across different scientific domains[45, 40]. Leveraging statistical independence of noise, first introduced in the work of Noise2Noise (N2N) [53] was given a theoretical grounding in the work of Noise2Self by posing it under a self-supervised framework [7]. Other approaches similar to N2S and N2N (such as Noise2Void, etc.) were also proposed around the same time [49, 50]. In this work, we introduce **Patch2Self (P2S)** [29] which belongs to this same family of algorithms and leverages the statistical independence of noise. P2S combines N2N and N2S and recasts the 4D self-supervised denoising of dMRI as an image in-painting problem [9]. Instead of holding out a part of the same 3D volume, P2S holds out the entire 3D volume itself and learns to predict a denoised version of the held-out volume as a linear combination of the remaining 3D volumes. P2S relies on the theory of $\mathcal{J}$-invariance [7, 29] to perform the denoising, which can be seen as a way of performing 4D image in-painting in the q-space [5]. In the case of dMRI data, denoising is typically done on a single subject and using P2S we show how one can get state-of-the-art denoising performance using linear regression as its backbone [13, 31, 75].

Self-supervised denoisers (typically making assumptions on the noise) outperform traditional methods of denoising, but can be computationally expensive as they do not place assumptions on signal properties such as sparsity, compressibility, repetition, etc. In pursuit of acquiring data at a higher resolution and to extract detailed diffusion information, the dimensionality of the data increases rapidly (per-volume and per-scan). Moreover, due to the advent of high-field scanners, more noise is induced in the signal due to the use of stronger magnetic gradients. Along with the dimensionality of a single scan, the number of scans acquired and released for analyses is also increasing rapidly, requiring fast and efficient denoising algorithms for clinical use.

To alleviate these issues, we also introduce **P2S-sketch**, which proposes the sketching of the large matrix $\mathcal{A}$ [29] constructed for training the denoiser via P2S to create a coreset. $\mathcal{A}$ is constructed by vectorizing each 3D volume and concatenating it along the columns of $\mathcal{A}$. This is called a *Casorati matrix* where each independent measurement forms a column of $\mathcal{A}$ [61]. So, instead of performing the self-supervised denoising on the over-determined set of constraints ($\mathcal{A} \in \mathbb{R}^{n \times d}$, where $n \gg d$), P2S-sketch samples and rescales the matrix to a much smaller subset of the constraints ($\mathcal{A} \in \mathbb{R}^{s \times d}$, where $n \gg s \approx d$). By training the self-supervised denoiser on this much smaller induced sub-problem, we show that one can achieve the same level of denoising performance as P2S with a highly reduced time complexity and a much smaller memory footprint. We show the speedup gains both via the theoretical complexity analysis and the empirical comparisons on simulated and real datasets of different dimensionalities. To ensure that P2S-sketch does not hamper the denoising performance, we compare P2S-sketch against P2S on both simulated and real data using the root mean squared error (RMSE) and the R^2 metrics. We also evaluate the performance on the downstream tasks of microstructure modeling and tractography. While the sketch size required for sketching and solving the linear system within P2S-sketch may vary, our experiments suggest at least a 60% redundancy in the training set. We compared the performance of P2S-sketch via different sketching methods such as CountSketch, leverage score sampling, and the Subsampled Randomized Fourier Transform (SRFT). Our results show that leverage score sampling yielded the best performance. We discuss how leverage scores can be used for interpretability of P2S-sketch, revealing which regions of the data have a higher influence on the denoising algorithm. This enables interpretability (crucial to medical imaging) of the self-supervised denoising, which is otherwise treated as a black-box approach. With the help of the Rank Revealing QR (RRQR) decomposition, we also show how one can calibrate the optimal sketch size to construct the coreset for P2S-sketch via a self-supervised loss.

2. Methods

In this paper, we introduce two algorithms P2S and P2S-sketch sequentially since P2S-sketch builds on top of P2S-sketch. The organization of the methods is such that each algorithm is preceded by the necessary preliminaries.

2.1. Patch2Self: Self-supervised Denoising of Diffusion MRI

2.1.1. Patches and Local Matrix Approximations

Patch-based self-supervision has been used to learn representations that are invariant to distortions [21, 20], for learning relations between patches [19], for filling in missing data (i.e. image in-painting) [67], etc. P2S abides by a similar patch-based approach where we learn an underlying clean signal representation that is invariant to random fluctuations in the observed signal. Inspired by the local matrix approximation works presented in [52, 11], we formulate a global estimator per 3D volume of the 4D data by training on local patches sampled from the remaining volumes. This estimator function, thus has access to local and non-local information to learn the mapping between corrupted signal and true signal, similar to dictionary learning [35, 74, 77, 37, 10] and non-local block matching [18]. Due to the self-supervised formulation, P2S can be viewed as a non-parametric method that regresses over patches from all other volumes except from the one that is held-out for denoising. Our experiments demonstrate that a simplistic linear-regression model can be used to denoise noisy matrices using p-neighbourhoods and a class of $\mathcal{J}$-invariant functions.

2.2. Denoising via Self-Supervised Local Approximations

Extracting 3D patches: In the first phase of P2S, we extract a p-neighbourhood for each voxel from the 4D DWI data. To do so, we construct a 3D block of radius p around each voxel, resulting in a local p-neighbourhood of dimension $p \times p \times p$.

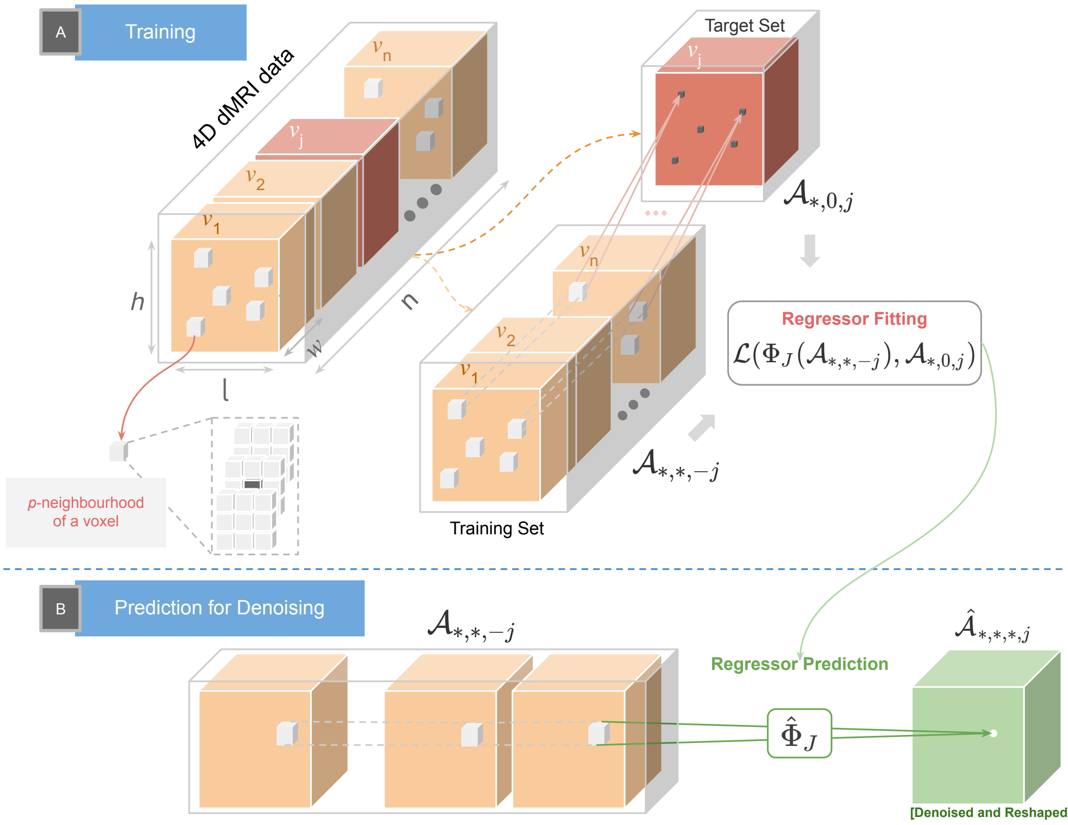

Figure 1: Depicts the workflow of Patch2Self in two phases: **(A)** Is the self-supervised training phase where the 4D DWI data is split into the training $\mathcal{A}_{*,*,-j}$ and target $\mathcal{A}_{*,0,j}$ sets. p-neighbourhoods are extracted from each 3D volume from both $\mathcal{A}_{*,*,-j}$ and $\mathcal{A}_{*,0,j}$. Φ_J is the learnt mapping by regressing over p-neighbourhoods of $\mathcal{A}_{*,*,-j}$ to estimate $\mathcal{A}_{*,0,j}$. **(B)** Depicts the voxel-by-voxel denoising phase where $\hat{\Phi}_J$ predicts the denoised volume $\hat{\mathcal{A}}_{*,*,*,j}$ from $\mathcal{A}_{*,*,-j}$.

Algorithm 1 Patch2Self

```
Input 4D data $\mathcal{A}$ of dimension $l \times w \times h \times d$
for volume $j = 1, 2, \ldots d$ [where $d$ is the number of volumes] do
    for voxel $k = 1, 2, \ldots m$ [where $m = lwh$ is the number of voxels] do
        Extract a $p \times p \times p$ neighbourhood of voxel $k$.
    Flatten and concatenate each $p$-neighbourhood into a feature vector of length $p^3 * n$.
Stack feature vectors into a matrix of size $m \times (p^3 \times n)$, to get Casorati matrix $\mathcal{A}$.
for volume $j = 1, 2, \ldots n$ do
    Hold-out features from volume $j$ to get a feature matrix $\mathcal{A}_{*,*,-j}$ $[m \times p^3 \times (n-1)]$
    Select the central pixels from volume $j$ to get a target vector $\mathcal{A}_{*,0,j}$ of dimension $m$.
    Train a regressor $\Phi : \mathcal{A}_{*,*,-j} \mapsto \mathcal{A}_{*,0,j}$.
    Set the denoised volume $\hat{\mathcal{A}}_{*,*,*,j}$ to the unraveled output $\hat{\Phi}(\mathcal{A}_{*,*,-j})$.
return Denoised 4D data $\hat{\mathcal{A}}$
```

Therefore, if the 4D DWI has n volumes $\{v_1, \ldots, v_n\}$ (each volume corresponding to a different gradient direction) and each 3D volume has m voxels (see Fig. 1), after extracting the p-neighbourhoods, we get a $m \times p \times p \times p \times n$ tensor. Next, we flatten this this tensor along the p^{th}-dimension to obtain a representation: $m \times (p^3 \times n)$. Thus, we have transformed the data from the original 4D space to obtain m samples of $p^3 \times n$ dimensional 2D feature matrices, which we use for denoising.

Self-Supervised Regression: In the second phase, using the p-neighbourhoods, P2S reformulates the problem of denoising with a predictive approach. The goal is to iterate and denoise each 3D volume of the noisy 4D DWI data using the following training and prediction phases:

(i) Training: To denoise a particular volume, v_j, we train the a regression function Φ_J using p-neighbourhoods of the voxels denoted by the set $\mathcal{A}$. From the first phase, $\mathcal{A}$ is a set containing m training samples with dimension: $p^3 \times n$. Next, we hold out the dimension corresponding to volume v_j from each of the p-neighbourhoods and use it as a target for training the regressor function Φ_J (shown in Fig. 1A). Therefore our training set $\mathcal{A}_{*,*,-j}$ has dimension: $m \times p^3 \times (n-1)$, where j indexes the held out dimension of the p-neighbourhoods set. Using the regressor function Φ_J, we use the training set $\mathcal{A}_{*,*,-j}$ to only predict the center voxel of the set of p-neighbourhoods in the corresponding target set of dimension $\mathcal{A}_{*,0,-j}$. The target set, is therefore only an m-dimensional vector of the center voxels of the corresponding p-neighbourhoods of volume v_j. In summary, we use the localized spatial neighbourhood information around each voxel of the set of volumes v_{-j}, to train Φ_J for approximating the center voxel of the target volume v_j. To do so, we propose minimizing the self-supervised loss over the described p-neighbourhood sets as follows:

$$\mathcal{L}(\Phi_J) = \mathbb{E}\|\Phi_J(\mathcal{A}_{*,*,-j}) - \mathcal{A}_{*,0,j}\|^2 \tag{1}$$

Where, $\Phi_J : \mathbb{R}^{p^3 \times n} \mapsto \mathbb{R}^1$, is trained on m samples of p-

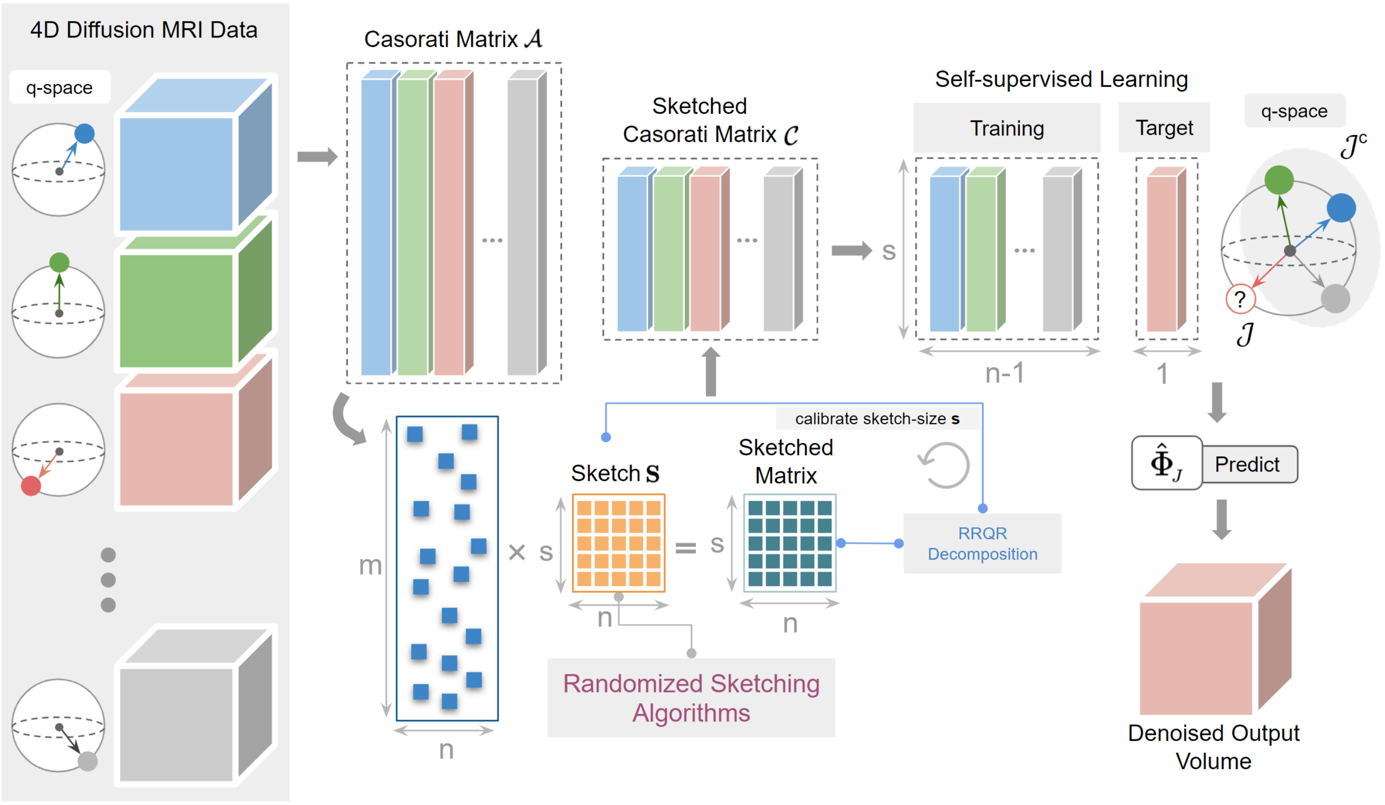

Figure 2: We show how Patch2Self2 works in the case of Diffusion MRI data. The Casorati Matrix $\mathcal{A}$ is constructed by flattening each gradient direction. $\mathcal{A}$ is then sketched via a randomized algorithm to generate the smaller sketched Casorati Matrix C. The $\mathcal{J}$-invariant training is then performed on C to learn $\hat{\Phi}_J$ and predict the denoised volume.

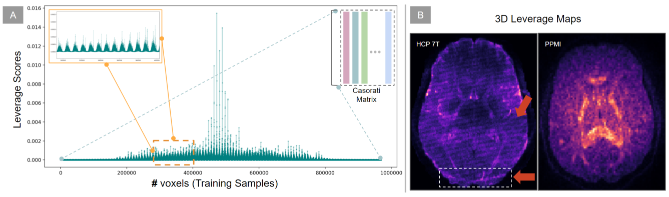

Figure 3: (A) We depict an exemplary point-plot of the row leverage scores computed on the Casorati matrix of a real dataset. (B) We show the axial slice of the 3D leverage score maps computed on two example datasets. Notice that the leverage score maps capture structured artefacts spatially correlated across gradient directions (indicated by red arrows on the HCP 7T data).

neighbourhoods.

(ii) Predict: After training for m samples, we have now constructed a $\mathcal{J}$-invariant regressor $\hat{\Phi}_J$ that can be used to denoise the held out volume v_j. To do so, p-neighbourhoods from the set $\mathcal{A}_{*,*,-j}$ are simply fed into $\hat{\Phi}_J$ to obtain the denoised p-neighbourhoods corresponding to the denoised volume $\hat{\mathcal{A}}_{*,0,-j}$. After doing so, for each $j \in \{1 \ldots n\}$, we unravel the p-neighbourhoods for each volume $v_j \in \{v_1 \ldots v_n\}$ (in Fig. 1 as $\hat{\mathcal{A}}_{*,*,*,j}$) and append them to get denoised 4D DWI data $\hat{\mathcal{A}}$ (Details in 1).

***$\mathcal{J}$-Invariance*:** The reason one might expect the regressors learned using the self-supervised loss above to be effective denoisers is the theory of $\mathcal{J}$-invariance introduced in [7]. Consider the partition of the data into volumes, $\mathcal{J} = \{v_1, \ldots, v_n\}$. If the noise in each volume is independent from the noise in each other volume, and a denoising function Φ satisfies the property that the output of Φ in volume v_j does not depend on the input to Φ in volume v_j, then according to Proposition 1 of [7], the sum over all volumes of the self-supervised losses in equation 1 will in expectation be equal to the ground-truth loss of the denoiser Φ, plus an additive constant. This means that $\mathcal{J}$-invariant functions minimizing the self-supervised loss will also minimize the ground-truth loss. This holds by construction for our denoiser $\Phi = (\Phi_1, \ldots, \Phi_n)$. Intuitively, each Φ_J only has access to the signal present in the volumes other than v_j, and since the noise in those volumes is irrelevant for predicting the noise in v_j, it will learn to suppress the fluctuations due to noise while preserving the signal. Note that, if linear regression is used to fit each Φ_J, then the final denoiser Φ is a linear function. Unlike methods which work by thresholding the singular values obtained from a local eigen-decomposition [58, 81], which produce denoised data that are locally low-rank, this mapping Φ can be full-rank.

Choice of Regressor: Any class of regressor can be fit in the above method, from simple linear regression/ordinary least squares to regularized linear models like Ridge and Lasso, to more complex nonlinear models. Our code-base allows for the use of any regression model from [68]. Surprisingly, we found that linear regression performed comparably to the more sophisticated models, and was of course faster to train (see supplement for comparisons).

Choice of Patch Radius: To determine the effect of changing the patch radius on denoising accuracy, we compute the Root Mean Squared Error (RMSE) between the ground truth and P2S denoised estimates at SNR 15 (details of simulation in supplement). For patch radius zero and one, we show the effect at different number of volumes. The line-plot trend in supplement shows that the difference in the RMSE scores between the two patch radii steadily decreases with an increase in number of volumes. However, with lesser number of volumes, a bigger patch-radius must be used. In the remainder of the text, we use and show results with patch radius zero and linear regressors.

To summarize, leveraging the fact that each 3D volume of the 4D data can be assumed to be an independent measurement of the same underlying object, P2S proposes constructing a large Casorati matrix wherein each column can be assumed to be linearly independent of the other columns. P2S sets up the self-supervised regression task so that each column is denoised by representing it as a combination of the remaining columns. For the sake of simplicity, we denote the self-supervised loss of P2S in the following form for the remainder of the text: $\mathcal{L}(\Phi_J) = \mathbb{E}\left\|\Phi_J\left(\mathcal{A}_{-j}\right) - \mathcal{A}_j\right\|_2^2$. Here $\mathcal{A}_j$ refers to the voxels corresponding to the volume that were held-out and used as target for training the rest of the voxels from the remaining 3D volumes $\mathcal{A}_{-j}$. P2S showed that this $\mathcal{J}$-invariant function was in fact a linear map $\Phi_J : \mathcal{A}_{-j} \mapsto \mathcal{A}_j$ that achieved the optimal denoising performance. This allows re-writing the P2S as a linear regression problem:

$$\min_{\mathbf{w}} \|\mathcal{A}_{-j}\mathbf{w} - \mathcal{A}_j\|_2^2, \tag{2}$$

where $\mathcal{A}_{-j} = \left[\mathbf{a}_\mathbf{1}^\top \dots, \mathbf{a}_\mathbf{n}^\top\right] \in \mathbb{R}^{n\times d-1}$ are the features of the design matrix, excluding the held-out j-th column. The target for learning Φ_J is the held out 3D volume $\mathcal{A}_j = \left[a_1^\top, \dots, a_n^\top\right] \in \mathbb{R}^n$.

2.3. Coresets for Regression via Matrix Sketching

The self-supervised denoising performed in P2S relies on least squares regression as described in Sec. Preliminaries and Approach. Linear regression typically performed via Cholesky, SVD or QR decomposition needs $O\left(nd^2\right)$ time. In the case of P2S, the problem setup via the Casorati matrix $\mathcal{A}$ is massively over-constrained, i.e., $n \gg d$, and has an added time complexity, since the regression is performed d times given that each volume needs to be separately denoised. Therefore, in P2S-sketch, instead of computing the exact solution vector $\mathbf{w}^*= \text{argmin}_\mathbf{w} \|\mathcal{A}_{-j}\mathbf{w} - \mathcal{A}_j\|_2^2$, we propose to approximate it using tools from randomized matrix multiplication and subspace embeddings. The key idea here is to solve a sub-problem $\widetilde{\mathbf{w}} = \text{argmin}_\mathbf{w} \|\mathbf{S}\mathcal{A}_{-j}\mathbf{w} - \mathbf{S}\mathcal{A}_j\|_2^2$ such that

$$\|\mathcal{A}_{-j}\widetilde{\mathbf{w}} - \mathcal{A}_j\|_2^2 \leq (1+\epsilon)\|\mathcal{A}_{-j}\mathbf{w}^* - \mathcal{A}_j\|_2^2, \tag{3}$$

where ϵ is the desired level of accuracy and $\mathbf{S} \in \mathbb{R}^{s\times n}$ with $d \approx s \ll n$ is the so-called *sketching matrix*. Given the linear sketch $\mathbf{S}\mathcal{A}_{-j}$ of $\mathcal{A}_{-j}$, note that computing $\widetilde{\mathbf{w}}$ takes $O(sd^2)$ time, which is indeed much faster than the classical computation of $\mathbf{w}^*$. Therefore, our goal is to work with a suitable $\mathbf{S}$ such that the sketch $\mathbf{S}\mathcal{A}_{-j}$ can be computed efficiently and satisfies eqn. (3) with high probability. There are several such choices for $\mathbf{S}$:

Count-sketch [14]: In this case, $\mathbf{S}$ is a sparse embedding matrix with $s = O(d^2/\epsilon)$ rows and has exactly one non-zero entry per column, which is chosen randomly and set to ±1 independently. The product $\mathbf{S}\mathcal{A}_{-j}$ can be computed in time $O(\mathsf{nnz}(\mathcal{A}_{-j}))$. Assuming the failure probability to be a constant, the overall running time to compute $\widetilde{\mathbf{w}}$ is given by $O(\mathsf{nnz}(\mathcal{A}_{-j}))+ \text{poly}(d/\epsilon)$. Here, $\mathsf{nnz}(\cdot)$ denotes the sparsity of the underlying matrix.

Fast Johnson-Lindenstrauss transformations [27, 15]: Other choices for the sketching matrix $\mathbf{S}$ include structured random matrices such as the subsampled randomized Fourier transform (SRFT) or the subsampled randomized Hadamard transform (SRHT). In these cases, the sketching matrix $\mathbf{S}$ is typically of the form $\mathbf{S} = \sqrt{\frac{n}{s}}\mathbf{RHD}$, where $\mathbf{D} \in \mathbb{R}^{n\times n}$ is a random diagonal matrix with the entries set to ±1 independently; $\mathbf{R} \in \mathbb{R}^{s\times n}$ is a subset of s rows of the $n \times n$ identity matrix chosen uniformly at random, independently, without replacement; and $\mathbf{H} \in \mathbb{R}^{n\times n}$ is either a normalized discrete Fourier transform (for SRFT) or a normalized Walsh-Hadamard matrix (for SRHT). Note that both SRFT and SRHT are based on randomized linear transformations, which can be applied rapidly to arbitrary vectors. Indeed, we can compute the matrix-matrix product $\mathbf{S}\mathcal{A}_{-j}$ in $O(nd\log n)$ time exploiting the structure of the underlying Fourier/Hadamard matrix; if $s = O(d + \log {}^1\!/\epsilon \log {}^d\!/\epsilon)$, then the resulting sketching matrix satisfies eqn. (3). The overall running time is $O(nd\log n) + \widetilde{O}(d^3/\epsilon^2)$.

Sampling-based sketching [26]: A third way of achieving a subspace embedding that satisfies eqn. (3) is data-dependent, and can be obtained by sampling rows of a matrix proportional to their leverage scores $\ell_i = \|\mathbf{U}_{i*}\|_2^2$ for $i = 1\dots n$, where $\mathbf{U}_{i*} \in \mathbb{R}^n$ is the i-th row of the matrix of the left singular vectors of $\mathcal{A}_{-j}$ that are computed using the thin SVD of $\mathcal{A}_{-j}$. In this context, the sketching matrix $\mathbf{S}$ is the so-called *sampling-and-rescaling* matrix of [22] with the sampling probabilities $p_i = {}^{\ell_i}\!/_d$, $i = 1\dots n$, and the sample complexity is given by $s = O({}^{d\log d}\!/_{\epsilon^2})$. We note that computing ℓ_is exactly needs access to the matrix $\mathbf{U}$ which is expensive. Therefore, in practice, approximate leverage scores also suffice and they can be efficiently computed without computing the matrix $\mathbf{U}$ [23, 14]. We also note that there is another line of work [2, 73] that used sketching as a randomized preconditioner to come up with high precision solutions for overconstrained regression problems. However, in context of P2S-sketch, we can achieve the desired accuracy in denoising performance, even with a *sketch-and-solve* approach as discussed above. Finally, we refer the interested reader to the surveys [85, 25, 54, 24, 60] for background on Randomized Linear Algebra.

3. Statistical Leverage for Interpretability

In the previous section, we described how leverage scores can be used to perform importance sampling in order to generate the coreset for P2S-sketch. Here we show how to use

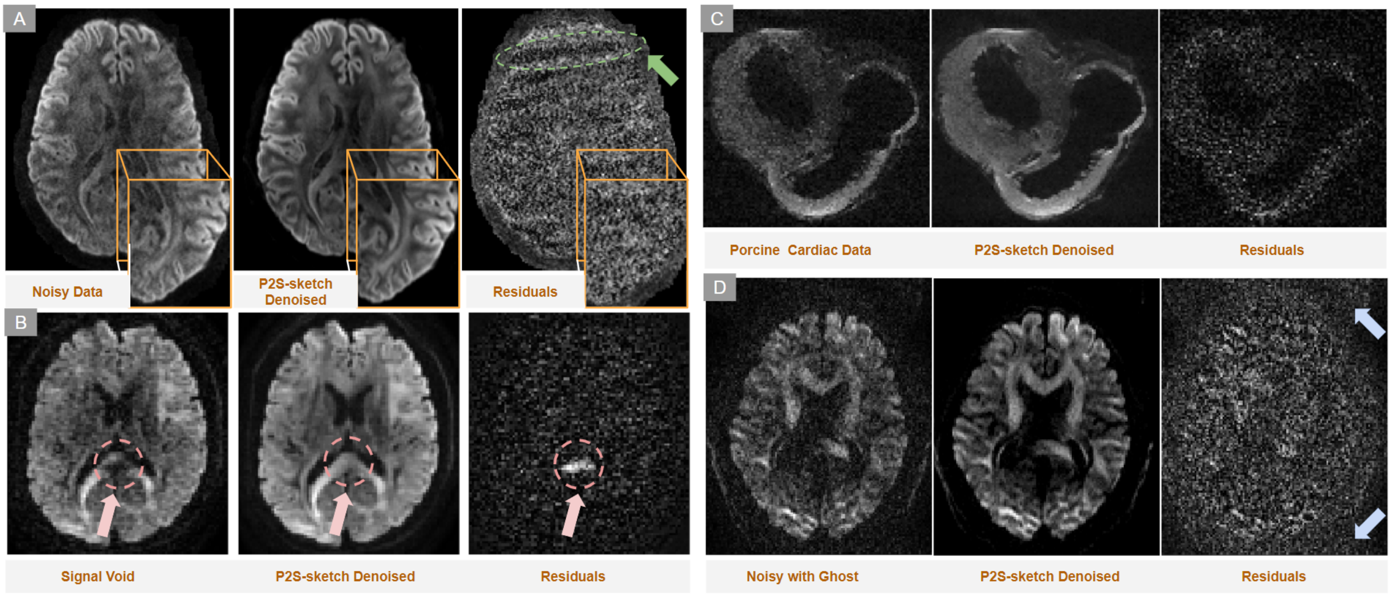

Figure 4: Depicts (A) Noisy band-like pattern in the residual maps suppressed via P2S-sketch (indicated by a green arrow). (B) In-painting of a signal void present in the original data and the predicted signal in the corresponding residual map (indicated by red arrows). (C) Capability of extending P2S-sketch to other organs such as the heart (Porcine Cardiac Data). (D) Suppression of ghosting artefacts (indicated by blue arrows).

the statistical leverage scores of the underlying linear model for interpreting areas of the data that influence the noise. From a statistical perspective, an alternative formulation of leverage scores are the diagonal entries of the projection matrix constructed to solve the linear regression [24, 55]. Typically, one looks at the standard deviation of the noise derived from the models used to perform the denoising [81]. Since P2S and consequently P2S-sketch are set up to denoise in a predictive setting via self-supervision, we can use statistical leverage to get a more detailed view of the factors that would influence the denoising performance. In Fig. 3A, we show the leverage scores computed on a subject from the PPMI dataset [59]. As one can see in the plot, some voxels in the data exhibit considerably higher statistical leverage. Voxels where an anatomical signal from the brain is captured exhibit higher leverage when compared to the voxels in the background, which have very small leverage scores. In Fig. 3B, we show the spatial map of leverage scores for two example datasets, PPMI and HCP 7T [80]. In the case of the PPMI data, we note that the regions of the white matter, such as the corpus callosum, have higher statistical leverage compared to the rest of the brain. Strikingly, we also see that a slanting structured pattern (indicated with red arrows) appears in the leverage scores map of the HCP 7T data. This structure can also be seen in the noise map of Fig. 4A in the residual map. Leverage score maps of the same HCP 7T subject also highlighted a structured artefact at the bottom of the axial slice (depicted as a white-dotted bounding box). It could be a ghost or a structured artefact added to the 7T data.

4. P2S-sketch Algorithm

P2S-sketch extends the idea of P2S (see Sec. Preliminaries and Approach) by performing self-supervised training on coresets. In case of dMRI, we have d number of 3D volumes each with dimensionality: $l \times w \times h$. Each of the volumes is flattened to a 1D array ($n = l{\times}w{\times}h$) to form a column of the Casorati matrix $\mathcal{A} \in \mathbb{R}^{n\times d}$. Next, we sketch this matrix $\mathcal{A}$ using the sketching matrix $\mathbf{S}(\in \mathbb{R}^{s\times n})$ to get a sketched Casorati matrix $C = \mathbf{S}\mathcal{A}$ (see Sec. Coresets for Regression via Matrix Sketching). We perform a self supervised denoising on this sketched matrix C by solving the sub-problem: $\min_{\widetilde{\mathbf{w}}} \|C_{-j}\mathbf{w} - C_j\|_2^2$. This denoising is performed on a volume-by-volume basis as proposed in P2S, where j corresponds to the volume held out for denoising. Thus, P2S-sketch learns a linear map $\Phi_J : \mathbb{R}^{s\times(d-1)} \mapsto \mathbb{R}^s$, which is a much smaller sub-problem to solve since $s \ll n$. After the training is done, the approximate solution vector $\widetilde{\mathbf{w}}$ learned via Φ_J is used to predict the held out volume of $\mathcal{A}_j$. In order to predict the denoised volume, the full Casorati matrix $\mathcal{A}_{-j}$ with all rows is given as input to the function Φ_J (Algorithm is further detailed in 2). In P2S-sketch, we allow switching between different sketching methods such as SRFT, leverage scores, and CountSketch (see Sec. Coresets for Regression via Matrix Sketching for details of each). Our results show that sketching via leverage scores outperforms other sketching methods (detailed comparison in Sec. Performance Comparison of Sketching Methods). As per the above procedure, P2S-sketch introduces using a new hyperparameter - the sketch size that needs to be tuned. We propose a $\mathcal{J}$-invariant self-supervised calibration procedure to find an optimal sketch size s based on the QR decomposition and leverage score sketching. Leverage scores are a univariate statistic. When two rows of $\mathcal{A}$ have identical or similar leverage scores, it implies that the rows are highly correlated and therefore redundant in the construction of the sketched Casorati matrix C. Thus, a redundancy removal step is often useful to reduce the sketch size s while retaining denoising performance. Towards that end, P2S-sketch employs the Rank Revealing QR (RRQR) factorization [38], to flag such redundancies by ranking the rows of the matrix in order of independence. In other words, highly linearly independent rows are given priority after the RRQR has been computed. In P2S-sketch, to calibrate the sketch size, we start with $s < 50\%$ of the number of rows in $\mathcal{A}$ and compute the rank-revealing QR (RRQR) decomposition [38] of C. The RRQR ranks the rows of C in order of importance and can be used to remove redundant rows from the sketched matrix. Next, as shown in Fig. 5A, we select the top k-ranked rows from C and compute the self-supervised loss. Gradually, by increasing the size of k in each iteration we compute the self-supervised loss for each iteration. The self-supervised loss for each value of k is computed as: $||\Phi_J(\mathcal{A}_{-j}) - \mathcal{A}_j||$. As shown in Fig. 5B, the loss eventually converges to a minimum with minimal change in the denoising performance. At that point, the elbow in the error plot (shown by the red box) reveals the number of redundant rows of the data, which allows us to estimate the (approximately) optimal s.

Leverage Score Sampling Strategies: We can obtain the sketched matrix C via leverage score sampling using the following two procedures: (1) Deterministically choosing top s leverage scores; (2) Randomized sampling based on leverage scores. From Fig. 3A, it is evident that only a few rows of the Casorati matrix have a very high leverage score in comparison with the remaining ones. These rows seem to have a higher influence on the denoising performance. As shown in Fig. 6A, the deterministic selection of the highest leverage scores consistently performs worse at all sketch sizes when compared to randomly sampling leverage scores. To investigate this effect, we compared the distribution of the rows corresponding to deterministically chosen top 20K leverage scores against the randomly sampled 20K rows. From the joint plot obtained by fitting a kernel density estimation shown in Fig. 6B, it can be seen that the distribution of the randomly sampled leverage scores forms a bi-modal distribution as opposed to the uni-modal distribution obtained from a deterministic selection of the top 20K leverage scores. This implies that the randomization in the sampling procedure helps denoising by using values that do not have a "high leverage".

5. Results

In this section we evaluate P2S and P2S-sketch sequentially since the purpose of evaluation of both algorithms is different. For P2S, we perform qualitative and quantitative comparisons on real and simulated data. While the results on the real data are included in the main text, the results on simulated data for P2S are added to the supplement for compactness and avoiding repetition from [29] and P2S-sketch evaluations. To evaluate the performance on real data, we qualitatively and quantitatively compare the effects of P2S and P2S-sketch denoising on the residual maps, microstructure modeling [65] and tractography [42]. We quantify the effect of different sketch sizes on the speed and accuracy of the approximate solution ($\widetilde{\mathbf{w}}$) in comparison with the P2S solution ($\mathbf{w}^*$).

Algorithm 2 Patch2Self-sketch

```
Input 4D data $X$ of dimension $l \times w \times h \times d$
for volume $j = 1, 2, \ldots d$ [where $d$ is the number of volumes] do
    Flatten volume $v_j$ to generate a feature vector of size $n$ [where $m = l \times w \times h$]
Stack feature vectors into a matrix of size $n \times d$ to generate the Casorati matrix $\mathcal{A}$.
Construct a random matrix $\mathbf{S}$ based on row leverage scores of $\mathcal{A}$, s.t. $\mathbf{S} \in \mathbb{R}^{s \times n}$
Compute a sketched Casorati matrix $C = \mathbf{S}\mathcal{A} \in \mathbb{R}^{s \times d}$
[Q, R, rank] = QR($C$) [where QR is the rank-revealing QR decomposition]
Select top $k$ rows of $C$ based on the rank [via self-supervised calibration] to form the matrix $\hat{C} \in \mathbb{R}^{k \times d}$
for volume $j = 1, 2, \ldots d$ do
    Hold-out features from volume $j$ to get a feature matrix $\hat{C}_{*,-j}$ of dimension $k \times (d-1)$
    Select the target volume $j$ to be denoised $\hat{C}_{*,j}$ of dimension $k \times 1$.
    Train a linear regressor $\Phi : \hat{C}_{*,-j} \mapsto \hat{C}_{*,j}$.
    Set the denoised volume $\hat{\mathcal{A}}_{*,*,*,j}$ to the unraveled output $\hat{\Phi}(\mathcal{A}_{*,-j})$.
return Denoised 4D data $\hat{\mathcal{A}}$
```

5.1. *Evaluation of P2S on in-vivo data*

We compare the performance of P2S with Marchenko-Pastur on the Parkinson's Progression Markers Initiative (PPMI) [59], Stanford HARDI [72] and Sherbrooke 3-Shell [33] datasets as shown in Fig. 6. These datasets represent different commonly used acquisition schemes: (1) Single-Shell (PPMI, 65 gradient directions), (2) High-Angular Resolution Diffusion Imaging (Stanford HARDI, 160 gradient directions) and (3) Multi-Shell (Sherbrooke 3-Shell, 193 gradient directions). For each of the datasets, we show the axial slice of a randomly chosen 3D volume and the corresponding residuals (squared differences between the noisy data and the denoised output). Note that both, Marchenko-Pastur and P2S, do not show any anatomical features in the error-residual maps, so it is likely that neither is introducing structural artifacts. P2S produced more visually coherent outputs, which is important as visual inspection is part of clinical diagnosis.

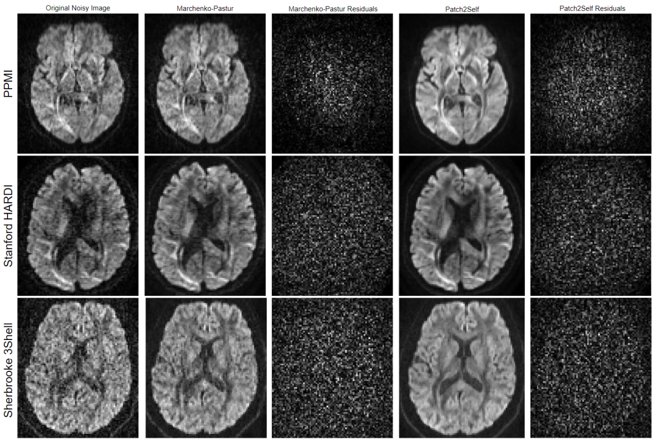

Figure 6: Shows the comparison of denoising on 3 different types of datasets: Parkinson's Progression Markers Initiative (PPMI), Stanford HARDI and Sherbrooke 3-Shell HARDI data. The denoising of P2S is compared against the original noisy image and Marchenko-Pastur denoised data along with their corresponding residuals. Notice that P2S suppresses more noise and also does not show any anatomical structure in the corresponding residual plots.

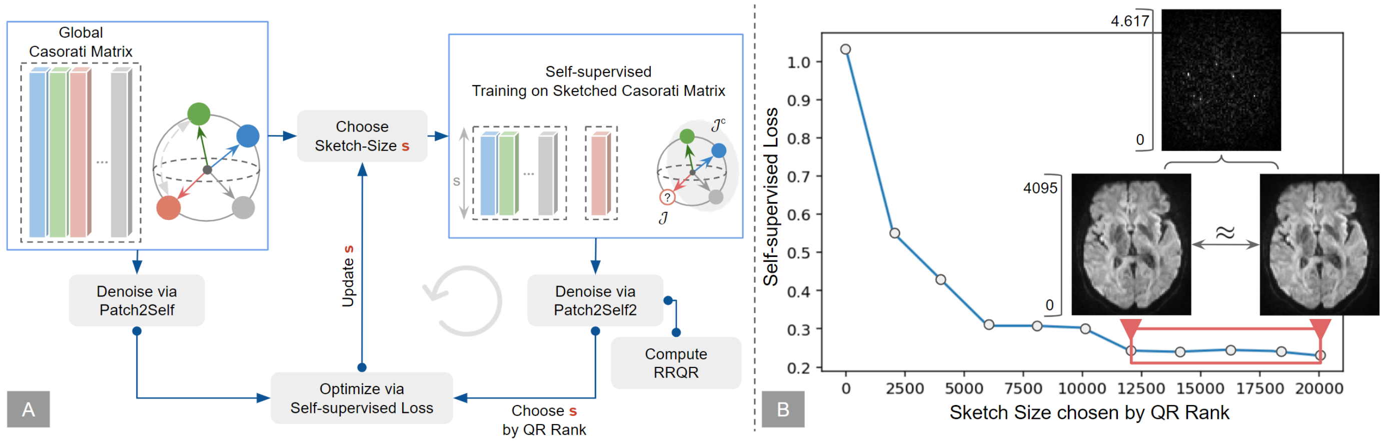

Figure 5: (A) Iterative self-supervised calibration procedure to obtain the optimal sketch size s to be used within P2S-sketch using a RRQR decomposition. the self-supervised loss is computed, by iteratively reducing the size of s until convergence. (B) We depict an example loss plot of the self-supervised calibration with exemplary PPMI data.

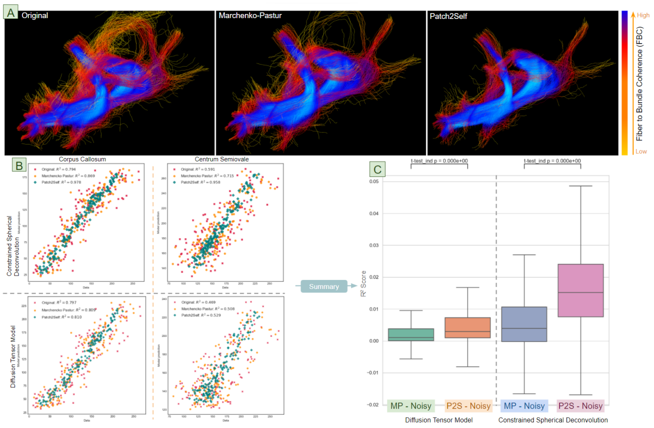

Figure 7: (A) Depicts the Fiber to Bundle Coherency (FBC) density map projected on the streamlines of the optic radiation bundle generated by the probabilistic tracking algorithm. The color of the streamlines depicts the coherency – *yellow* corresponding to incoherent and *blue* corresponding to coherent. Notice that the number of incoherent streamlines present in the original fiber-bundle is reduced after Marchenko-Pastur denoising. P2S denoising further reduces spurious tracts, resulting in a cleaner representation of the fiber bundle. (B) Quantitative comparison of the goodness-of-fit evaluated using a cross-validation approach. Depict the scatter plots of the model predictions obtained by fitting CSD to voxels in the corpus callosum (CC) and centrum semiovale (CSO) for original (noisy), Marchenko-Pastur (denoised) and P2S (denoised) data. Similarly, also show the scatter plots of predictions obtained from DTI fitting in the same voxel locations. Top-left of each plot shows the R^2 metric computed from each model fit on the corresponding data. (C) Boxplots quantifying the increase in R^2 metric after fitting downstream DTI and CSD models. The R^2 improvements in each case are plotted by subtracting the scores of model fitting on noisy data from R^2 of fitting each denoised output. Note that the consistency of microstructure model fitting on P2S denoised data is higher than that obtained from Marchenko-Pastur (see 5.3 for details and significance).

5.2. *Effect of P2S on Tractography*

To reconstruct white-matter pathways in the brain, one integrates orientation information of the underlying axonal bundles (streamlines) obtained by decomposing the signal in each voxel using a microstructure model [8, 65]. Noise that corrupts the acquired DWI may impact the tractography results, leading to spurious streamlines generated by the tracking algorithm. We evaluate the effects of denoising on probabilistic tracking [34] using the Fiber Bundle Coherency (FBC) metric [69]. To perform the probabilistic tracking, the data was first fitted with the Constant Solid Angle (CSA) model [1]. The Generalized Fractional Anisotropy (GFA) metric extracted from this fitting was used as a stopping criterion within the probabilistic tracking algorithm. The fiber orientation distribution information required to perform the tracking was obtained from the Constrained Spherical Deconvolution (CSD) [78] model fitted to the same data. In Fig. 7A, we show the effect of denoising on tractography for the Optic Radiation (OR) bundle as in [69]. The OR fiber bundle, which connects the visual cortex:V1 (calcarine sulcus) to the lateral geniculate nucleus (LGN), was obtained by selecting a 3×3×3 Region Of Interest (ROI) using a seeding density of 6. After the streamlines were generated, their coherency was measured with the local FBC algorithm [69, 28]), with *yellow-orange* representing - spurious/incoherent fibers and *red-blue* representing valid/coherent fibers. In Fig, 7, OR bundle tracked from original/ raw data contains 3114 streamlines, Marchenko-Pastur denoised data [81] contains 2331 streamlines and P2S denoised data contains 1622 streamlines. P2S outperforms Marchenko-Pastur by reducing the number of incoherent streamlines, as can be seen in the *red-blue* (depicting high coherence) coloring in Fig. 7A.

5.3. *Impact of P2S on Microstructure Model Fitting*

The domain of microstructure modeling employs either mechanistic or phenomenological approaches to resolve tissue structure at a sub-voxel scale. Fitting these models to the data is a hard inverse problem and often leads to degenerate parameter estimates due to the low SNR of DWI acquisitions [64]. We apply two of the most commonly used diffusion microstructure models, Constrained Spherical Deconvolution (CSD) [78] and Diffusion Tensor Imaging (DTI) [6], on raw and denosied data. DTI is a simpler model that captures the local diffusion information within each voxel by modeling it in the form of a 6-

parameter tensor. CSD is a more complex model using a spherical harmonic representation of the underlying fiber orientation distributions. In order to compare the goodness of each fit, we perform a k-fold cross-validation (CV) [39] at two exemplary voxel locations, corpus callosum (CC), a single-fiber structure, and centrum semiovale (CSO), a crossing-fiber structure. The data is divided into $k = 3$ different subsets for the selected voxels, and data from two folds are used to fit the model, which predicts the data on the held-out fold. The scatter plots of CV predictions against the original data are shown in Fig. 7B for those two voxels. As measured by R^2, P2S has a better goodness-of-fit than Marchenko-Pastur by 22% for CC and 65% for CSO. To show that P2S consistently improves model fitting across all voxels, in Fig. 7C we depict the improvement of the R^2 metric obtained from the same procedure for the axial slice (4606 voxels) of masked data (using [72] data). This was done by simply subtracting the goodness-of-fit R^2 scores of fitting noisy data, from Marchenko-Pastur and P2S denoised data for both CSD and DTI models. P2S shows a significant improvement on both DTI and CSD (two-sided t-test, $p <$ 1e-300, Fig. 7C). In order to evaluate the improvement of model fitting, we compared the residuals after fitting the DTI model both before and after denoising. To do so, we made use of 60 subjects from the LA5c cohort (30 controls and 30 schizophrenics) and compared the improvement of residuals after denoising and fitting the DTI model. As one can see via Fig. 10, P2S reduces the residual error much more than MPPCA. The comparison was done by computing the mean absolute error of the residuals between the raw and denoised images to quantify the improvement of model fitting after denoising. Now that we have shown of the noise suppression of P2S, we shift the focus towards P2S-sketch where we start with evaluating different sketching methods and benchmark its performance against P2S. We adopt the same evaluation scheme as P2S [30] where we show similar performance of P2S-sketch against P2S-sketch on denoising performance, microstructure and tractography.

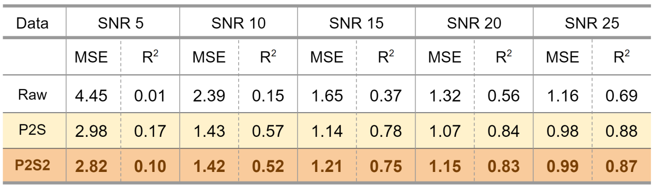

Data	SNR 5		SNR 10		SNR 15		SNR 20		SNR 25	
	MSE	R^2	MSE	R^2	MSE	R^2	MSE	R^2	MSE	R^2
Raw	4.45	0.01	2.39	0.15	1.65	0.37	1.32	0.56	1.16	0.69
P2S	2.98	0.17	1.43	0.57	1.14	0.78	1.07	0.84	0.98	0.88
P2S2	**2.82**	**0.10**	**1.42**	**0.52**	**1.21**	**0.75**	**1.15**	**0.83**	**0.99**	**0.87**

Table. 1: Quantitative comparison of Raw, P2S and P2S-sketch denoised data via MSE and R^2 metrics.

5.4. Performance Comparison of Sketching Methods within P2S-sketch

The P2S-sketch algorithm follows a sketch-and-solve [26, 82] approach and therefore the sketch size can affect the denoising performance. In order to quantify this effect, we chose a random subject from the PPMI dataset which was acquired with a widely used 64-directions DTI protocol. A random volume (here vol. #11) from this data was first denoised with P2S and the solution $\mathbf{w}^*$ obtained from it was treated as the optimal solution. Each volume of this subject contained around 960K voxels. Starting with a sketch size of 500 samples, P2S-sketch denoising was performed on the data with sketches computed using CountSketch, leverage score sampling and SRFT algorithms explained in Sec. Coresets for Regression via Matrix Sketching. The sketch size was then increased iteratively until the approximate solution $\widetilde{\mathbf{w}}$ was numerically very close to $\mathbf{w}^*$. The relative error for each iteration and method was computed as: $\frac{||\mathbf{w}^*-\widetilde{\mathbf{w}}||_2}{||\mathbf{w}^*||_2}$.This procedure was repeated ten times to capture the variance of denoising performance since the underlying algorithms used to approximate the solution are randomized. The variance with a 95% confidence interval was plotted at each iteration (i.e., for each sketch size). We also compared the performance of the sketching methods with uniform sampling and with the deterministic choice of the rows corresponding to the top leverage scores, for the same sketching sizes. As shown in Fig. 6A, the variance of all the sampling algorithms is reduced as the sketch size increases. Uniform sampling and deterministic leverage scores perform worse than the randomized algorithms at each sketch size. While CountSketch and leverage score sampling perform approximately the same, leverage score sampling performs slightly better and offers the added advantage of interpretability. In Fig. 6C, we also empirically compare the speedup obtained from P2S-sketch in comparison with P2S. This supplements our theoretical complexity analysis in Sec. Coresets for Regression via Matrix Sketching. With experiments on three different datasets we note that the speedup obtained increases as the sketch size reduces. We also find that the speedup obtained via P2S-sketch increases in proportion to the dimensionality of the data. As one can see in Fig. 6C, the speedup on the Stanford HARDI data (shape: $81 \times 106 \times 76 \times 160$) is much more than simulated (shape: $256\times256\times\times4\times63$) and PPMI data (shape: $116\times116\times72\times65$). The QR decomposition computed as a part of self-supervised calibration in P2S-sketch does not add a significant computational overhead. The wall-clock time on an i7 CPU with 16GB RAM for the QR decomposition took 0.0904s on a sketch-size of 20k which amounts to 20% of the PPMI data [59] that the calibration was run on (see Fig.5). So if the experiment was to be run 10 times for calibration, the QR computation would take $< 1s$, as the subsequent runs would have fewer than 20k rows.

5.5. Impacts of P2S-sketch on Microstructure and Tractography

To estimate the underlying tissue **microstructure** in the living brain one typically fits a biophysical model to each voxel of the dMRI data to capture tissue heterogeneity. Diffusion kurtosis imaging (DKI) [43] is one such modeling scheme that quantifies the degree of non-Gaussian diffusion. DKI is however sensitive to noise and can often lead to fitting degeneracy in the derived maps. In Fig. 8A, we show that P2S alleviates this issue by significantly reducing the failures of model fitting in the data. We also show that P2S-sketch provides very similar estimates of the derived DKI metrics, here, radial (RK) and mean (MK) kurtosis. The same HCP 7T data was used to evaluate the DKI measures in the presence of band-like structured noise. We note that the raw noisy data shows the banded noisy artefacts on the

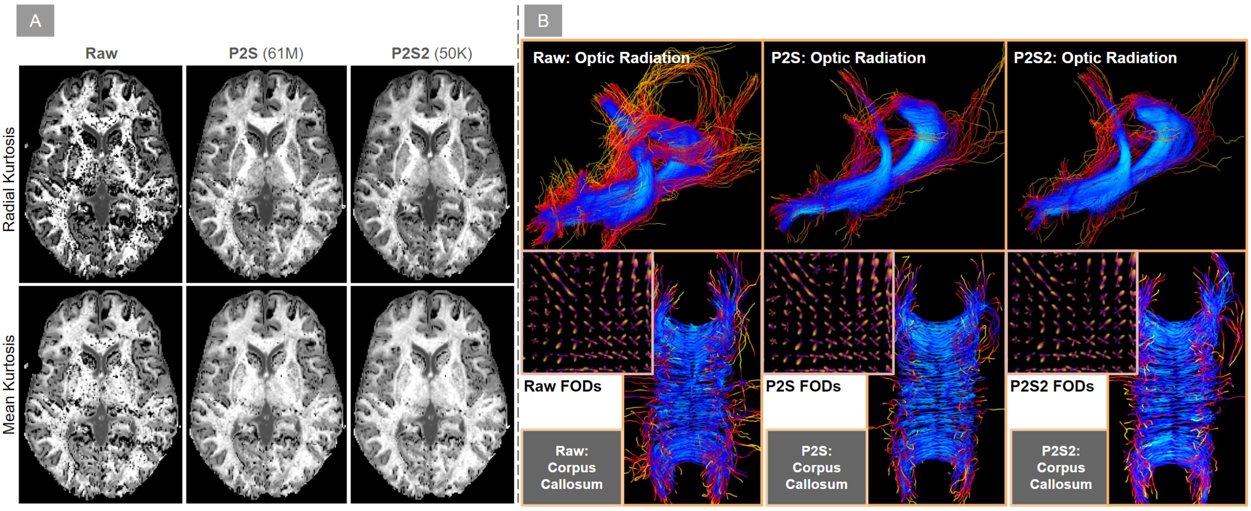

Figure 8: (A) Quantifies the effect of P2S and P2S-sketch denoising on HCP 7T data modeled using Diffusion Kurtosis (DKI). Derived Radial Kurtosis and Mean Kurtosis metrics are shown for both P2S and P2S-sketch. (B) We compare the performance of P2S-sketch with P2S and noisy data via fiber-to-bundle coherence quantification of the optic radiation and corpus callosum bundles. Also shows a cross-section of underlying spherical harmonic representations (FODs).

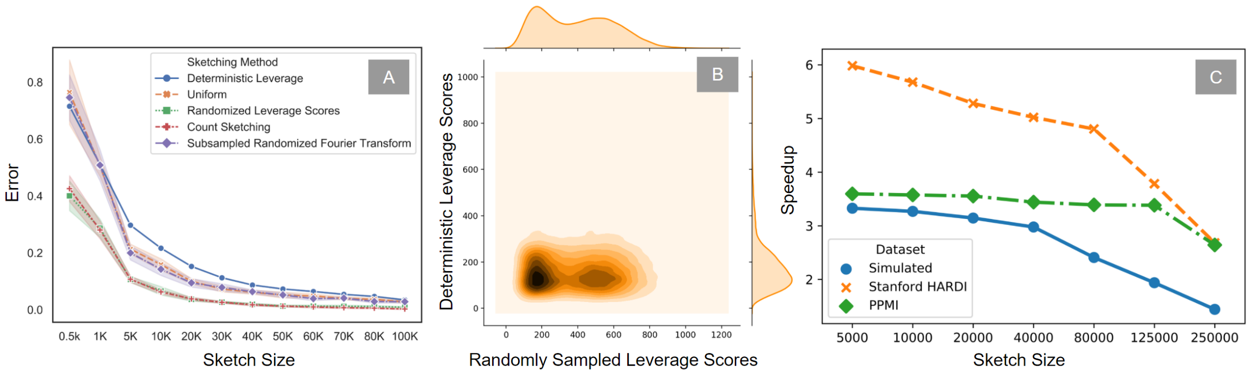

Figure 6: (A) We quantify the error variance in the approximation of the P2S-sketch solution vector when compared to P2S. Three different randomized algorithms (CountSketch, leverage score sampling and SRFT) are compared with uniform sampling and the deterministic choice of the rows corresponding to the largest leverage scores. (B) Joint kernel density estimate plot of the 20K voxels: randomly sampled according to leverage scores vs. deterministically chosen. (C) Shows empirical speedup comparisons (against P2S) on three different datasets, by incrementally increasing the sketch size.

derived DKI metrics. In order to gauge the effect of denoising, the RK and MK metrics were used to evaluate the denoising performance. Both P2S and P2S-sketch yield very similar results although P2S-sketch was trained on only 50K of the 61M samples (0.083%) of the raw data (goodness of fit comparisons in supplement). We employ the exact same procedure (with the same parameters) described in Sec. 5.2 to compare P2S-sketch against P2S for effects on tractography. In Fig. 8B we show the effect of denoising via P2S and P2S-sketch on the fiber orientation distribution (FOD) plotted via the CSD model. To denoise via P2S-sketch, only 50K samples out of the 6M (8.3%) samples were used in the training process. Note that both P2S and P2S-sketch suppress noisy lobes uncovering the underlying fiber crossings. The generalized fractional anisotropy obtained from the constrained solid angle algorithm [1] was used as the stopping criterion of the probabilistic tracking. Next, the streamlines tracking the optic radiation and corpus callosum bundles, obtained from noisy, P2S denoised and P2S-sketch denoised data, were quantified using the fiber-to-bundle coherence metric [69] shown in Fig. 8B. The red-yellow streamlines depict the spurious and incoherent streamlines while the blue ones depict the coherent and true representative streamlines. Since the probabilistic tracking algorithm is stochastic in nature, some variability in the streamlines is expected, but both P2S and P2S-sketch yield very similar results.

5.6. *Evaluation of P2S-sketch on Simulated Data*

To compare performance on simulated data, we use a strategy similar to the one proposed in P2S (see supplement) [29, 84, 36]. The data was simulated with 2 b0 (*non-dMRI*) volumes and 60 diffusion-weighted dMRI volumes. 30 of these dMRI volumes had a b-value of 1000 s/mm^2 and the remaining 30 with 2000 s/mm^2. An 8-channel coil sensitivity map was used to add Gaussian noise to the real and imaginary part of each channel to simulate realistic Rician noise. Sum-of-square coil scheme was used to combine the data and the SNR was calculated in the white-matter of the b0 image. Altogether, six datasets were simulated: noise-free and SNR equal to 10, 15, 20, 25, and 30. For each SNR, we denoised the data using P2S and P2S-sketch. We compare the denoising performance of both algorithms qualitatively and quantitatively. We see that both P2S and P2S-sketch yield visually very similar results as shown in Fig. 9A. In order to quantify the difference, we compute the root mean squared error and the R^2 metric between the denoised data and the ground truth at each SNR, for both P2S and P2S-sketch. The results are shown in Tab. 1. The denoising performance of P2S-sketch performance very closely approximates the denoised data obtained via P2S. Both P2S and P2S-sketch proportionally improve their performance as the SNR increases. This can also be seen in the scatter plots of signal intensities from noisy data, with P2S and P2S-sketch results shown at SNRs equal to 15 and 20 (see Fig. 9B) depicted via P2S and P2S-sketch overlap almost perfectly.

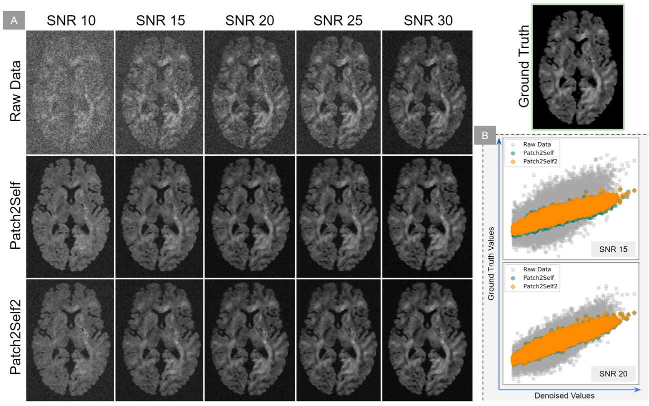

Figure 9: Shows (A) Qualitative comparison of denoising performance between P2S and P2S-sketch (trained on 20K samples, i.e. 7% of the data). (B) P2S-sketch closely approximates P2S via scatter plots at SNRs 15&20.

5.7. *Noise suppression and artefact removal*

Visual conspicuity of the data (i.e. image quality) is crucial to any form of medical imaging, especially dMRI where the images are inherently limited by SNR. While thermal noise is known to dominate the sources of noise that corrupt the underlying signal [81], different acquisition strategies tend to induce different types of artefacts that hamper the signal structure. We show that the self-supervised setup of P2S-sketch deals with these artefacts without loss of signal corresponding to anatomical structure. In Fig. 4A, we denoised a subject **HCP 7T** dataset [80] using only 50K out of 61M (0.083%) training samples obtained via leverage score sampling. Noise mapping from this type of high-field imaging data (acquired using 7 Tesla scanner) is still under-investigated. We show that P2S-sketch suppressed band-like structured noise, which may be correlated across some volumes, but is largely uncorrelated across all 3D volumes. One of the main motives of high-field 7T scanners is to acquire data at a much higher resolution. With a zoomed-in cross-section in Fig. 4A, we show how P2S-sketch uncovers much more anatomical detail without loss of information or contrast. **Signal voids** are a common issue in MRI that occur due to certain voxels not emitting any radio-frequency signal due to a lack of activated protons in that region [83]. Since P2S, and consequently P2S-sketch, are similar to image in-painting [9], where an entire 3D volume is predicted as a combination of the rest of the volumes, this signal void can be imputed with context learned from the rest of the volumes. This setup resolves a unique issue for dMRI data which was not addressed by any other denoising algorithm in the past. In Fig. 4B we show how P2S-sketch fills the signal void present in the Stanford HARDI [72] data in gradient direction 33, without removing or smoothing the signal in the rest of the image. In Fig. 4C,D we show how P2S-sketch does not cause any signal loss even in the presence of physiological noise (porcine cardiac data) [32, 63] and ghost artefacts [70, 51], which are ubiquitous in MRI acquisitions. Note that in either case, P2S-sketch strictly only suppresses noise and does not lead to signal loss or smoothing. [In the supplement, we compare the P2S-sketch residuals with P2S].

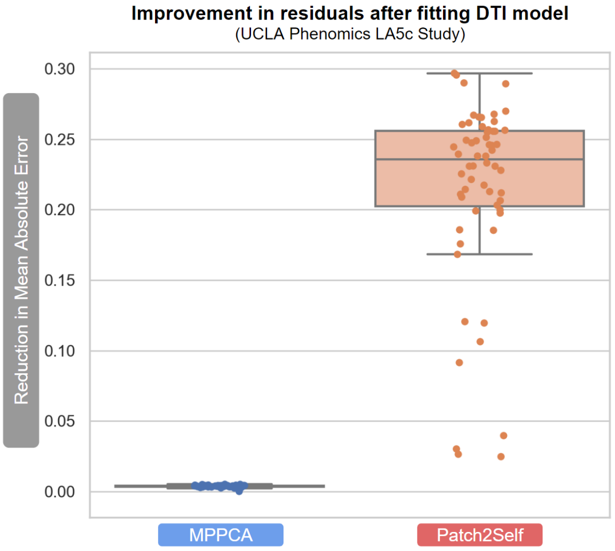

Figure 10: Comparison of improvement in the residuals after DTI fitting after denoising via MPPCA and P2S. Notice that P2S reduces the residual error for all 60 subjects used from the LA5c cohort in comparison with MPPCA.

6. Conclusions

This paper proposes a new method for denoising dMRI data, which is usually acquired at a low SNR, for the purpose of improving microstructure modeling, tractography, and other downstream tasks. We demonstrated that denoising by P2S outperforms the state-of-the-art random-matrix-theory-based Marchenko-Pastur method on these subsequent analyses. To enable broad adoption of this method by the MRI community, we have incorporated an efficient and unit-tested implementation of Patch2Self into the widely-used open-source library DIPY [33]. In this work we also proposed Patch2Self-sketch which performs self-supervised denoising using coresets constructed via matrix sketching, resulting in significant speedups and reduced memory usage. Our results showed that sampling-based sketching via leverage scores gave the best performance. Remarkably, leverage scores can be directly used as a statistic for interpreting influential regions hampering the denoising performance. Patch2Self-sketch will be released as a part of DIPY and a separate Pythonic matrix sketching package.

References

[1] Iman Aganj, Christophe Lenglet, Guillermo Sapiro, Essa Yacoub, Kamil Ugurbil, and Noam Harel. Reconstruction of the orientation distribution function in single and multiple shell q-ball imaging within constant solid angle. *Magnetic Resonance in Medicine*, 2009.

[2] Haim Avron, Petar Maymounkov, and Sivan Toledo. Blendenpik: Supercharging LAPACK's least-squares solver. *SIAM Journal on Scientific Computing*, 32(3):1217–1236, 2010.

[3] Suyash P Awate and Ross T Whitaker. Feature-preserving MRI denoising: a nonparametric empirical bayes approach. *IEEE Transactions on Medical Imaging*, 26(9):1242–1255, 2007.

[4] Hubert Banville, Omar Chehab, Aapo Hyvärinen, Denis-Alexander Engemann, and Alexandre Gramfort. Uncovering the structure of clinical eeg signals with self-supervised learning. *Journal of Neural Engineering*, 18(4):046020, 2021.

[5] Peter J Basser. Relationships between diffusion tensor and q-space mri. *Magnetic Resonance in Medicine: An Official Journal of the International Society for Magnetic Resonance in Medicine*, 47(2):392–397, 2002.

[6] P.j. Basser, J. Mattiello, and D. Lebihan. MR diffusion tensor spectroscopy and imaging. *Biophysical Journal*, 66(1):259–267, 1994.

[7] Joshua Batson and Loic Royer. Noise2Self: Blind denoising by self-supervision. In *Proceedings of the 36th International Conference on Machine Learning*, volume 97 of *Proceedings of Machine Learning Research*, pages 524–533. PMLR, 2019.

[8] Timothy E.j. Behrens and Saad Jbabdi. MR diffusion tractography. *Diffusion MRI*, page 333–351, 2009.

[9] Marcelo Bertalmio, Guillermo Sapiro, Vincent Caselles, and Coloma Ballester. Image inpainting. In *Proceedings of the 27th annual conference on Computer graphics and interactive techniques*, pages 417–424, 2000.

[10] Berkin Bilgic, Kawin Setsompop, Julien Cohen-Adad, Anastasia Yendiki, Lawrence L Wald, and Elfar Adalsteinsson. Accelerated diffusion spectrum imaging with compressed sensing using adaptive dictionaries. *Magnetic Resonance in Medicine*, 68(6):1747–1754, 2012.

[11] Emmanuel J. Candes and Terence Tao. The power of convex relaxation: Near-optimal matrix completion. *IEEE Transactions on Information Theory*, 56(5):2053–2080, 2010.

[12] Geng Chen, Yafeng Wu, Dinggang Shen, and Pew-Thian Yap. Xq-nlm: denoising diffusion MRI data via x-q space non-local patch matching. In *International Conference on Medical Image Computing and Computer-Assisted Intervention*, pages 587–595. Springer, 2016.

[13] Matthew Cieslak, Philip A Cook, Xiaosong He, Fang-Cheng Yeh, Thijs Dhollander, Azeez Adebimpe, Geoffrey K Aguirre, Danielle S Bassett, Richard F Betzel, Josiane Bourque, et al. Qsiprep: an integrative platform for preprocessing and reconstructing diffusion mri data. *Nature methods*, 18(7):775–778, 2021.

[14] Kenneth L Clarkson and David P Woodruff. Low-rank approximation and regression in input sparsity time. *Journal of the ACM (JACM)*, 63(6):1–45, 2017.

[15] Michael B. Cohen, Jelani Nelson, and David P. Woodruff. Optimal Approximate Matrix Product in Terms of Stable Rank. In *43rd International Colloquium on Automata, Languages, and Programming (ICALP 2016)*, volume 55, pages 11:1–11:14, 2016.

[16] P. Coupe, J.V. Manjon, M. Robles, and D.L. Collins. Adaptive multiresolution non-local means filter for three-dimensional magnetic resonance image denoising. *IET Image Processing*, 6(5):558, 2012.

[17] P. Coupe, P. Yger, S. Prima, P. Hellier, C. Kervrann, and C. Barillot. An optimized blockwise nonlocal means denoising filter for 3-d magnetic resonance images. *IEEE Transactions on Medical Imaging*, 27(4):425–441, 2008.

[18] Kostadin Dabov, Alessandro Foi, Vladimir Katkovnik, and Karen Egiazarian. Image denoising with block-matching and 3D filtering. In Nasser M. Nasrabadi, Syed A. Rizvi, Edward R. Dougherty, Jaakko T. Astola, and Karen O. Egiazarian, editors, *Image Processing: Algorithms and Systems, Neural Networks, and Machine Learning*, volume 6064, pages 354 – 365. International Society for Optics and Photonics, SPIE, 2006.

[19] Carl Doersch, Abhinav Gupta, and Alexei A. Efros. Unsupervised visual representation learning by context prediction, 2015.

[20] Alexey Dosovitskiy, Philipp Fischer, Jost Tobias Springenberg, Martin Riedmiller, and Thomas Brox. Discriminative unsupervised feature learning with exemplar convolutional neural networks, 2014.

[21] Alexey Dosovitskiy, Jost Tobias Springenberg, Martin Riedmiller, and Thomas Brox. Discriminative unsupervised feature learning with convolutional neural networks. In Z. Ghahramani, M. Welling, C. Cortes, N. D. Lawrence, and K. Q. Weinberger, editors, *Advances in Neural Information Processing Systems 27*, pages 766–774. Curran Associates, Inc., 2014.

[22] Petros Drineas, Ravi Kannan, and Michael W Mahoney. Fast monte carlo algorithms for matrices i: Approximating matrix multiplication. *SIAM Journal on Computing*, 36(1):132–157, 2006.

[23] Petros Drineas, Malik Magdon-Ismail, Michael W. Mahoney, and David P. Woodruff. Fast approximation of matrix coherence and statistical leverage. *Journal of Machine Learning Research*, 13(111):3475–3506, 2012.

[24] Petros Drineas and Michael W. Mahoney. RandNLA: Randomized numerical linear algebra. *Communications of the ACM*, 59(6):80–90, 2016.

[25] Petros Drineas and Michael W. Mahoney. *Lectures on randomized numerical linear algebra*, volume 25 of *The Mathematics of Data, IAS/Park City Mathematics Series*. American Mathematical Society, 2018.

[26] Petros Drineas, Michael W Mahoney, and Shan Muthukrishnan. Sampling algorithms for l_2 regression and applications. In *Proceedings of the seventeenth annual ACM-SIAM symposium on Discrete algorithm*, pages 1127–1136, 2006.

[27] Petros Drineas, Michael W Mahoney, Shan Muthukrishnan, and Tamás Sarlós. Faster least squares approximation. *Numerische mathematik*, 117(2):219–249, 2011.

[28] Remco Duits and Erik Franken. Left-invariant diffusions on the space of positions and orientations and their application to crossing-preserving smoothing of hardi images. *International Journal of Computer Vision*, 92(3):231–264, 2010.

[29] Shreyas Fadnavis, Joshua Batson, and Eleftherios Garyfallidis. Patch2self: Denoising diffusion MRI with self-supervised learning. In H. Larochelle, M. Ranzato, R. Hadsell, M. F. Balcan, and H. Lin, editors, *Advances in Neural Information Processing Systems*, volume 33, pages 16293–16303. Curran Associates, Inc., 2020.

[30] Shreyas Fadnavis, Marco Reisert, Hamza Farooq, Maryam Afzali, Cheng Hu, Bago Amirbekian, and Eleftherios Garyfallidis. Microlearn: Framework for machine learning, reconstruction, optimization and microstructure modeling. *International Symposium on Magnetic Resonance in Medicine (ISMRM'19)*, 09 2019.

[31] Shreyas Fadnavis, Jens Sjölund, Anders Eklund, and Eleftherios Garyfallidis. Nuq: A noise metric for diffusion mri via uncertainty discrepancy quantification. *arXiv preprint arXiv:2203.01921*, 2022.

[32] Pedro F Ferreira, Sonia Nielles-Vallespin, Andrew D Scott, Ranil de Silva, Philip J Kilner, Daniel B Ennis, Daniel A Auger, Jonathan D Suever, Xiaodong Zhong, Bruce S Spottiswoode, et al. Evaluation of the impact of strain correction on the orientation of cardiac diffusion tensors with in vivo and ex vivo porcine hearts. *Magnetic resonance in medicine*, 79(4):2205–2215, 2018.

[33] Eleftherios Garyfallidis, Matthew Brett, Bagrat Amirbekian, Ariel Rokem, Stefan Van Der Walt, Maxime Descoteaux, and Ian and Nimmo-Smith. Dipy, a library for the analysis of diffusion MRI data. *Frontiers in Neuroinformatics*, 8, 2014.

[34] Gabriel Girard, Kevin Whittingstall, Rachid Deriche, and Maxime Descoteaux. Towards quantitative connectivity analysis: reducing tractography biases. *NeuroImage*, 98:266–278, 2014.

[35] Alona Golts and Michael Elad. Linearized kernel dictionary learning. *IEEE Journal of Selected Topics in Signal Processing*, 10(4):726–739, 2016.

[36] Mark S. Graham, Ivana Drobnjak, and Hui Zhang. Realistic simulation of artefacts in diffusion MRI for validating post-processing correction techniques. *NeuroImage*, 125:1079–1094, 2016.

[37] Alexandre Gramfort, Cyril Poupon, and Maxime Descoteaux. Denoising and fast diffusion imaging with physically constrained sparse dictionary learning. *Medical image analysis*, 18(1):36–49, 2014.

[38] Ming Gu and Stanley C Eisenstat. Efficient algorithms for computing a strong rank-revealing qr factorization. *SIAM Journal on Scientific Com-*

puting, 17(4):848–869, 1996.

[39] Trevor Hastie, Jerome Friedman, and Robert Tisbshirani. *The Elements of statistical learning: data mining, inference, and prediction*. Springer, 2017.

[40] Allard Adriaan Hendriksen, Daniël Maria Pelt, and K Joost Batenburg. Noise2inverse: Self-supervised deep convolutional denoising for tomography. *IEEE Transactions on Computational Imaging*, 6:1320–1335, 2020.

[41] Rafael N Henriques, Marco Palombo, Sune N Jespersen, Noam Shemesh, Henrik Lundell, and Andrada Ianuş. Double diffusion encoding and applications for biomedical imaging. *Journal of Neuroscience Methods*, page 108989, 2020.

[42] Saad Jbabdi and Heidi Johansen-Berg. Tractography: where do we go from here? *Brain connectivity*, 1(3):169–183, 2011.

[43] Jens H. Jensen and Joseph A. Helpern. MRI quantification of non-gaussian water diffusion by kurtosis analysis. *NMR in Biomedicine*, 23(7):698–710, 2010.

[44] Derek K Jones. *Diffusion MRI*. Oxford University Press, 2010.

[45] Wesley Khademi, Sonia Rao, Clare Minnerath, Guy Hagen, and Jonathan Ventura. Self-supervised poisson-gaussian denoising. In *Proceedings of the IEEE/CVF Winter Conference on Applications of Computer Vision (WACV)*, pages 2131–2139, January 2021.

[46] Florian Knoll, Kristian Bredies, Thomas Pock, and Rudolf Stollberger. Second order total generalized variation (tgv) for MRI. *Magnetic Resonance in Medicine*, 65(2):480–491, 2010.

[47] Cheng Guan Koay, Evren Özarslan, and Peter J. Basser. A signal transformational framework for breaking the noise floor and its applications in MRI. *Journal of Magnetic Resonance*, 197(2):108–119, 2009.

[48] Lisa Sophie Kölln, Omar Salem, Jessica Valli, Carsten Gram Hansen, and Gail McConnell. Label2label: Using deep learning and dual-labelling to retrieve cellular structures in fluorescence images. *bioRxiv*, 2020.

[49] Alexander Krull, Tim-Oliver Buchholz, and Florian Jug. Noise2void - learning denoising from single noisy images, 2018.

[50] Samuli Laine, Tero Karras, Jaakko Lehtinen, and Timo Aila. High-quality self-supervised deep image denoising, 2019.

[51] Denis Le Bihan, Cyril Poupon, Alexis Amadon, and Franck Lethimonnier. Artifacts and pitfalls in diffusion MRI. *Journal of Magnetic Resonance Imaging: An Official Journal of the International Society for Magnetic Resonance in Medicine*, 24(3):478–488, 2006.

[52] Joonseok Lee, Seungyeon Kim, Guy Lebanon, Yoram Singer, and Samy Bengio. Llorma: Local low-rank matrix approximation. *Journal of Machine Learning Research*, 17(15):1–24, 2016.

[53] Jaakko Lehtinen, Jacob Munkberg, Jon Hasselgren, Samuli Laine, Tero Karras, Miika Aittala, and Timo Aila. Noise2noise: Learning image restoration without clean data. In *ICML*, pages 2971–2980, 2018.

[54] Michael W. Mahoney. Randomized algorithms for matrices and data. *Foundations and Trends in Machine Learning*, 3(2):123–224, 2011.

[55] Michael W Mahoney and Petros Drineas. Cur matrix decompositions for improved data analysis. *Proceedings of the National Academy of Sciences*, 106(3):697–702, 2009.

[56] Devraj Mandal, Shrisha Bharadwaj, and Soma Biswas. A novel self-supervised re-labeling approach for training with noisy labels. In *Proceedings of the IEEE/CVF Winter Conference on Applications of Computer Vision*, pages 1381–1390, 2020.

[57] José V. Manjón, Pierrick Coupé, Antonio Buades, D. Louis Collins, and Montserrat Robles. New methods for MRI denoising based on sparseness and self-similarity. *Medical Image Analysis*, 16(1):18–27, 2012.

[58] José V. Manjón, Pierrick Coupé, Luis Concha, Antonio Buades, D. Louis Collins, and Montserrat Robles. Diffusion weighted image denoising using overcomplete local pca. *PLoS ONE*, 8(9), 2013.

[59] Kenneth Marek, Danna Jennings, Shirley Lasch, Andrew Siderowf, Caroline Tanner, Tanya Simuni, Chris Coffey, Karl Kieburtz, Emily Flagg, Sohini Chowdhury, et al. The parkinson progression marker initiative (ppmi). *Progress in neurobiology*, 95(4):629–635, 2011.

[60] Per-Gunnar Martinsson and Joel Tropp. Randomized numerical linear algebra: Foundations & algorithms. *arXiv preprint arXiv:2002.01387*, 2020.

[61] Steen Moeller, Pramod Pisharady Kumar, Jesper Andersson, Mehmet Akcakaya, Noam Harel, Ruoyun Ma, Xiaoping Wu, Essa Yacoub, Christophe Lenglet, and Kamil Ugurbil. Diffusion imaging in the post hcp era. *Journal of Magnetic Resonance Imaging*, 2020.

[62] Pedro Morgado, Ishan Misra, and Nuno Vasconcelos. Robust audio-visual instance discrimination. *arXiv preprint arXiv:2103.15916*, 2021.

[63] Kévin Moulin, Ilya A Verzhbinsky, Nyasha G Maforo, Luigi E Perotti, and Daniel B Ennis. Probing cardiomyocyte mobility with multi-phase cardiac diffusion tensor MRI. *PloS one*, 15(11):e0241996, 2020.

[64] Dmitry S. Novikov, Valerij G. Kiselev, and Sune N. Jespersen. On modeling. *Magnetic Resonance in Medicine*, 79(6):3172–3193, Jan 2018.

[65] Dmitry S Novikov, Valerij G Kiselev, and Sune N Jespersen. On modeling. *Magnetic resonance in medicine*, 79(6):3172–3193, 2018.

[66] V. M. Pai, S. Rapacchi, P. Kellman, P. Croisille, and H. Wen. Pcatmip: Enhancing signal intensity in diffusion-weighted magnetic resonance imaging. *Magnetic Resonance in Medicine*, 65(6):1611–1619, 2010.

[67] Deepak Pathak, Philipp Krahenbuhl, Jeff Donahue, Trevor Darrell, and Alexei A. Efros. Context encoders: Feature learning by inpainting, 2016.

[68] F. Pedregosa, G. Varoquaux, A. Gramfort, V. Michel, B. Thirion, O. Grisel, M. Blondel, P. Prettenhofer, R. Weiss, V. Dubourg, J. Vanderplas, A. Passos, D. Cournapeau, M. Brucher, M. Perrot, and E. Duchesnay. Scikit-learn: Machine learning in Python. *Journal of Machine Learning Research*, 12:2825–2830, 2011.

[69] J. M. Portegies, R. H. J. Fick, G. R. Sanguinetti, S. P. L. Meesters, G. Girard, and R. Duits. Improving fiber alignment in hardi by combining contextual pde flow with constrained spherical deconvolution. *Plos One*, 10(10), 2015.

[70] David A Porter, Fernando Calamante, David G Gadian, and Alan Connelly. The effect of residual nyquist ghost in quantitative echo-planar diffusion imaging. *Magnetic Resonance in Medicine: An Official Journal of the International Society for Magnetic Resonance in Medicine*, 42(2):385–392, 1999.

[71] Alexis Reymbaut and Maxime Descoteaux. Advanced encoding methods in diffusion MRI. *arXiv preprint arXiv:1908.04177*, 2019.

[72] Ariel Rokem. Stanford hardi surfaces, Oct 2016.

[73] Vladimir Rokhlin and Mark Tygert. A fast randomized algorithm for overdetermined linear least-squares regression. *Proceedings of the National Academy of Sciences*, 105(36):13212–13217, 2008.

[74] Meyer Scetbon, Michael Elad, and Peyman Milanfar. Deep k-svd denoising, 2019.

[75] Kurt G Schilling, Shreyas Fadnavis, Mereze Visagie, Eleftherios Garyfallidis, Bennett A Landman, Seth A Smith, and Kristin P O'Grady. Patch2self denoising of diffusion mri in the cervical spinal cord improves repeatability and feature conspicuity. In *International Society for Magnetic Resonance in Medicine Annual Meeting*, 2021.

[76] Samuel St-Jean, Pierrick Coupé, and Maxime Descoteaux. Non local spatial and angular matching: Enabling higher spatial resolution diffusion MRI datasets through adaptive denoising. *Medical Image Analysis*, 32:115–130, 2016.

[77] Jeremias Sulam, Boaz Ophir, Michael Zibulevsky, and Michael Elad. Trainlets: Dictionary learning in high dimensions. *IEEE Transactions on Signal Processing*, 64(12):3180–3193, Jun 2016.

[78] J-Donald Tournier, Fernando Calamante, and Alan Connelly. Robust determination of the fibre orientation distribution in diffusion MRI: Non-negativity constrained super-resolved spherical deconvolution. *NeuroImage*, 35(4):1459–1472, 2007.

[79] Antonio Tristán-Vega and Santiago Aja-Fernández. Dwi filtering using joint information for dti and hardi. *Medical image analysis*, 14(2):205–218, 2010.

[80] David C Van Essen, Kamil Ugurbil, Edward Auerbach, Deanna Barch, Timothy EJ Behrens, Richard Bucholz, Acer Chang, Liyong Chen, Maurizio Corbetta, Sandra W Curtiss, et al. The human connectome project: a data acquisition perspective. *Neuroimage*, 62(4):2222–2231, 2012.

[81] Jelle Veraart, Dmitry S. Novikov, Daan Christiaens, Benjamin Ades-Aron, Jan Sijbers, and Els Fieremans. Denoising of diffusion MRI using random matrix theory. *NeuroImage*, 142:394–406, 2016.

[82] Shusen Wang, Alex Gittens, and Michael W Mahoney. Sketched ridge regression: Optimization perspective, statistical perspective, and model averaging. In *International Conference on Machine Learning*, pages 3608–3616. PMLR, 2017.

[83] Van J Wedeen, Robert M Weisskoff, and Brigitte P Poncelet. MRI signal void due to in-plane motion is all-or-none. *Magnetic resonance in medicine*, 32(1):116–120, 1994.

[84] Qiuting Wen, Mark Graham, Sourajit Mustafi, Ivana Drobnjak, Hui Zhang, and Yu-Chien Wu. Comparing the LPCA and MPPCA denoising

approaches for diffusion MRI using simulated human data. *International Society for Magnetic Resonance in Medicine*, 2017.

[85] David P. Woodruff. Sketching as a tool for numerical linear algebra. *Foundations and Trends in Theoretical Computer Science*, 10(1-2), 2014.

[86] Jure Zbontar, Li Jing, Ishan Misra, Yann LeCun, and Stéphane Deny. Barlow twins: Self-supervised learning via redundancy reduction. *arXiv preprint arXiv:2103.03230*, 2021.